Research Square

Preprints are preliminary reports that have not undergone peer review.
They should not be considered conclusive, used to inform clinical practice,
or referenced by the media as validated information.

Quantitative Digital Tapho-geochemistry of Upper Permian Petrified Wood from Paraguay: Multi-phase Permineralisation Resolved via High-Resolution µCT and Molecular Spectroscopy

Enrique Baez

filadelfia9108geologo@gmail.com

Centre for Applied Ecology of the Littoral (CONICET–UNNE)

Alexandra Crisafulli

Centre for Applied Ecology of the Littoral (CONICET–UNNE)

Agustín Kanbour

Faculty of Natural Sciences, National University of Salta (FCN–UNSa)

Christian Bulman Hartkopf

Agricultural Experiment Station, National Institute of Agricultural Technology (EEA-INTA).

Nestor Salinas Franco

Faculty of Exact and Natural Sciences, National University of Asunción (FACEN–UNA)

Diego López

Faculty of Exact and Natural Sciences, National University of Asunción (FACEN–UNA)

Moisés Gadea

Faculty of Exact and Natural Sciences, National University of Asunción (FACEN–UNA)

Research Article

Keywords: Baieroxylon cicatricum, diagenesis, digital petrography, mineralogy, µCT

Posted Date: February 26th, 2026

DOI: https://doi.org/10.21203/rs.3.rs-8855590/v1

License: This work is licensed under a Creative Commons Attribution 4.0 International License.
Read Full License

Additional Declarations: No competing interests reported.

Quantitative Digital Tapho-geochemistry of Upper Permian Petrified Wood from Paraguay: Multi-phase Permineralisation Resolved via High-Resolution μCT and Molecular Spectroscopy

Enrique Baez[1,2], Alexandra Crisafulli[1,2], Agustín Kanbour[3], Christian Bulman Hartkopf[4], Nestor Salinas Franco[5], Diego López[5], Moisés Gadea[5]

filadelfia9108geologo@gmail.com, alexandracrisafulli@hotmail.com, agustinkanbour@gmail.com, bulman.christian@inta.gob.ar, nestorsalinas@gmail.com, dlopez@facen.una.py, moi7moses@yahoo.com

1. Centre for Applied Ecology of the Littoral (CONICET–UNNE), Corrientes Province, Argentina, Laboratory 13 (Palaeoxylology and Palaeobotany).
2. Faculty of Exact and Natural Sciences and Surveying, National University of the Northeast (FaCENA-UNNE), Corrientes Province, Argentina, Department of Biology.
3. Faculty of Natural Sciences, National University of Salta (FCN–UNSa), Salta Province, Argentina, Department of Geology.
4. Agricultural Experiment Station, National Institute of Agricultural Technology (EEA-INTA)., Monte Carlo, Misiones Province, Argentina, Electron Microscopy and X-ray Analysis Laboratory.
5. Faculty of Exact and Natural Sciences, National University of Asunción (FACEN–UNA), University Campus, San Lorenzo, Central Department, Paraguay, Department of Geology.

*Corresponding author at: Facultad de Ciencias Exactas, Naturales y Agrimensura, Universidad Nacional del Nordeste, Corrientes - Centro de Ecología Aplicada del Litoral, Corrientes, Argentina. E-mail: filadelfia9108geologo@gmail.com (Enrique Baez).

Abstract.

The reconstruction of the three-dimensional mineralogical and anatomical architecture of fossil plants is essential for understanding Palaeozoic taphonomic processes. This study presents a high-resolution characterisation of *Baieroxylon cicatricum* (Ginkgoales) from the Upper Permian Tacuary Formation of the Independencia Group, exposed at Arroyo Vino (Gauirá Departament, eastern Paraguay), within the Guaireña Basin. Utilising X-ray micro-computed tomography (μCT) with an isotropic voxel size of 10 μm, the secondary xylem was digitally reconstructed to evaluate mineral density gradients through 16-bit attenuation mapping. These data were cross-validated using SEM-BSE-EDS and Confocal Raman Spectroscopy (CRS) to establish a comprehensive paragenetic sequence. The results reveal a multi-phase permineralisation history. The primary stage involved the volumetric replacement of woody tissues by stable alpha-quartz and hematite clusters (55.5 wt% Fe), stabilising the cellular morphostructure. A subsequent metasomatic event introduced metastable silica polymorphs, specifically monoclinic moganite and opal microspheres, into residual void spaces. The spatial distribution of opal within the 3D quartz framework, confirmed by Raman shifts at 787, 978, and 1587 cm^{-1}, indicates that the specimen remained geochemically active post-lithification. Furthermore, the detection of chromium (7.56% Cr) and uranium suggests that mineralising fluids were influenced by tectonic faulting within the Gondwanan Paraná Basin. The preservation of vestigial carbonaceous matter (14.1 wt%) confirms the efficiency of silica replacement in encapsulating primary biological relicts. This study marks a shift from

descriptive palaeoxylology to quantitative digital tapho-geochemistry, establishing a new diagnostic framework for interpreting complex mineralisation processes and reinforcing the palaeoenvironmental and palaeobiogeographical context of Gondwanan Permian floras.

Keywords: *Baieroxylon cicatricum*; diagenesis; digital petrography; mineralogy; μCT.

1. Introduction

The preservation of Permian wood evidences complex interactions between primary plant tissues, mineralising fluids, and post-burial geochemical regimes; however, the three-dimensional internal organisation of numerous paleoxylotaphofloras remains insufficiently delineated. This article presents and analyses the physicochemical and mineralogical characterisation of the three-dimensional morphostructure of *Baieroxylon cicatricum* Prasad and Lele, originating from the fossil locality Arroyo Vino, in the Colonia Independencia district, Department of Guairá, eastern Paraguay, where Upper Permian sediments corresponding to the Tacuary Formation, Independencia Group (Crisafulli and Herbst, 2009), are exposed. The various techniques applied in this study have enabled substantial advances in the mineralogical understanding of silicified fossilised petrified woods.

The SEM-EDS technique identifies major and trace elements within the wood, indicating partial mineralisation characterised by amorphous silica and residual fossil organic matter (Saminpanya *et al*., 2024). Mineral replacement occurs molecule by molecule across cell walls, tracheid lumina, intercellular spaces, and voids, predominantly associated with abundant iron oxide phases. Confocal Raman spectroscopy (CRS) utilises inelastic photon scattering to yield molecular-scale insights into silicon–oxygen tetrahedra in minerals, identifiable through vibrational, rotational, and low-frequency modes within silica systems (Viney *et al*., 2016). CRS was employed here to elucidate mineral assemblages, documenting quartz, opal, moganite, hematite, and preserved fossil organic matter.

Micro-computed tomography (μCT) revealed the three-dimensional microstructure of the permineralised wood, quantifying tomographic parameters voxel resolution, slice increment, and volumetric scaling with micrometre-scale precision. This study represents the first integrated three-dimensional characterisation of Paraguayan fossil wood, combining μCT imaging with phase-contrast mineralogical analyses. The results highlight the spatial heterogeneity of the lignified matrix, discriminating crystalline quartz overgrowths and amorphous silica infills, while resolving tracheidal morphology and, in part, diagenetic textures related to the infilling of internal cavities.

1.1 Background on mineralogical studies of fossil woods

García Giménez *et al*. (1983) investigated the mineralogy of Permian woods buried and fossilised by volcaniclastic materials, proposing that the silicifying fluids were derived from residual magmatic sources associated with a tectonic basin. Witke *et al*. (2004) examined silicified woods from the Lower Permian petrified forest of Chemnitz (Germany), analysing different types of permineralised plant remains using a range of microanalytical techniques, including scanning electron microscopy (SEM) and Raman spectroscopy. Their study identified distinctions between quartz and moganite, iron oxides at different oxidation states, and secondary minerals such as calcite and barite. Rafferty (2011) described metasomatic replacement as a coupled process of dissolution and precipitation, whereby one mineral replaces another, constituting a fundamental mechanism in wood petrification. More recently, studies

applying μCT scanning to palaeobotanical materials, together with mineralogical characterisation of fossil plant morphostructures, have significantly advanced the understanding of silicification and other complex mineralisation processes (Matsunaga *et al*., 2019; Calo *et al*., 2020). MicroCT techniques provide detailed microstructural and spatial distribution data on mineral specimens that were previously unattainable using conventional analytical approaches (Barron, 2024).

1.2 Background on xylological studies in Paraguay

In Paraguay, systematic xylogical investigations of petrified wood remain limited. Harrington (1950) and Eckel (1959) documented occurrences of fossil wood attributed to *Dadoxylon*. Herbst (1972, 1981) assigned an Upper Permian age to specimens from the Tacuary Formation, correlating them with the Estrada Nova Formation of Brazil on the basis of shared palaeoecological attributes (Runnegar and Newell, 1971). The Permian age of this unit was subsequently corroborated by studies by Muff *et al*. (1999) and Rapalini *et al*. (2006).

Within the Independencia Group, Herbst (1972) documented representatives of Lycopsidae incertae sedis attributed to the "Sigillariaceae". Several stems, collected approximately 130 km north of Siraty, were reported as indeterminate Lycopodopsidaceae, including cf. *Phyllotheca* sp. (Herbst, 1972) and *Cyclodendron* cf. *leslii* (Seward) Kräusel (Herbst, 1981). Additional significant records comprise arborescent ferns assigned to the genera *Guairea*, *Pasaronius*, and *Tuvichapteris*, as identified by Herbst (1987). Subsequently, Crisafulli (2000, 2004) examined gymnosperm woods from the Tacuary Formation. Within this unit, Crisafulli and Herbst (2009) described *Baieroxylon cicatricum*, the taxon investigated in this study. This species was originally established from the Tiki Formation (Triassic, India) by Prasad and Lele (1984) and later recognised by Crisafulli (2001) in the Yaguarí Formation (Permian, Uruguay). Further contributions by Leiva Verón *et al*. (2012) and Vallejos Leiz *et al*. (2018) document silicified woods of Coniferales and Ginkgoales from Siraty, Guavira, and the Tacuary Formation.

2. Geological and geographical setting

2.1 Geographical setting

The analysed specimen was recovered from the fossiliferous locality of Arroyo Vino, situated near the Tebicuary-mí River, between the settlements of Colonia Independencia and Melgarejo, in the northern sector of the Colonia Independencia district, Department of Guairá, Eastern Paraguay. The type area of the stratigraphic unit, as defined by Crisafulli and Herbst (2009), is located at 25°40′22″S and 56°13′20″W (Fig. 1). The Guairá Department is commonly referred to as the "Southern Corridor", reflecting its geographic position between two major sedimentary basins bounded by the Ybyturuzú and San Rafael ranges. This region occupies the central portion of Eastern Paraguay and is bordered by the Caaguazú Department to the north, Paraguarí to the west, and Caazapá to the south-east (Bartrina, 2007).

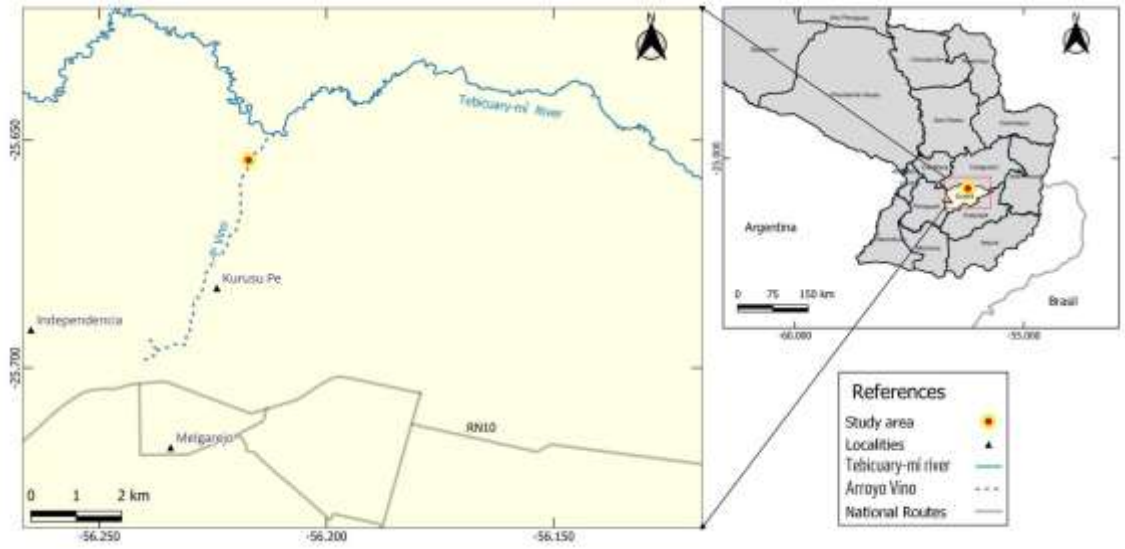


Figure 1. Location of the fossiliferous Arroyo Vino site in the northern sector of the Colonia Independencia district, Department of Guairá, Eastern Paraguay.

2.2 Tectonic framework

During the Neoproterozoic, Paraguay developed a tectonic configuration characterised by north-west–south-east and north-east–south-west structural trends, generated during the Brasiliano tectono-magmatic cycle, which spanned from the Proterozoic to the Lower Ordovician. These structural patterns were subsequently accentuated by epeirogenic reactivations during the Caledonian (Silurian) and Eohercynian (Carboniferous) orogenic phases (Gohrbandt, 1992; Velázquez *et al*., 1996). In particular, north-south and east-west oriented crystalline basement systems induced minor compressional events within the regional framework, recorded by stratigraphic unconformities, with structural alignments further enhanced during Mesozoic extensional tectonism (Hales, 1980). East–west displacement was additionally influenced by the South Atlantic thermotectonic cycle and later reactivated under similar orientations during the Cenozoic Andean thermotectonic phase (Almeida and Hasui, 1984; Wiens, 2018). The present stratigraphic architecture and outcrop distribution of Eastern Paraguay reflect this Palaeozoic–Mesozoic tectonic evolution, with sedimentary basins displaying thicknesses from approximately 100 m over structural highs to nearly 6000 m within the San Pedro Depression (Fúlfaro, 1996). Furthermore, the Phanerozoic succession of Eastern Paraguay comprises two major basins: one containing Ordovician–Silurian deposits and another dominated by Devonian sediments accumulated along a convergent margin, where subduction of the palaeo-Pacific plate beneath Gondwana generated a large cratonic depocentre, the Paraná Basin, subsequently infilled by Permo-Carboniferous successions (Fulfaro *et al*., 1982; Gohrbandt, 1992).

The Independencia Group developed in response to isostatic uplift affecting eastern Paraguay during the Permian. Contemporaneously, its Brazilian equivalent was deposited as the Palermo Formation within the Paraná Basin during the Late Permian (Litherland and Bloomfield, 1981). The Permo-Carboniferous succession is preserved within a fault-bounded zone characterised by a dominant northwest-trending structural grain, with an overall north–south extension, and rests unconformably upon Precambrian, Silurian, and Devonian substrata. The Jejuí-Guazú Fault delineates the boundary of all pre-Palaeozoic units north of the San Pedro aulacogen and coincides with the northern termination of the Independencia Group (Fig.

2) (Fúlfaro, 1996). Lithostratigraphically, the Independencia Group comprises four formations, namely the San Miguel, Tacuary, Tapytá, and Cabacuá formations (Wiens, 1982).

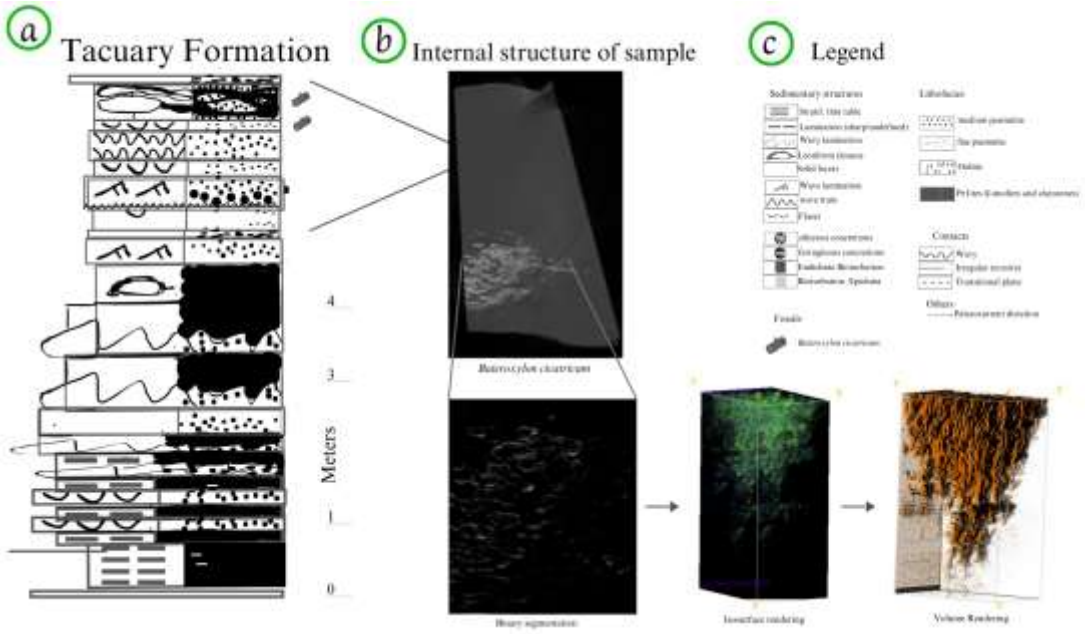


Figure 2. (a) Lithostratigraphic profile of the Tacuary Formation. (b) Internal anatomical structure of the taxon *Baieroxylon cicatricum*. (c) Processed images derived from X-ray microtomography scans.

The lithology of the Tacuary Formation is characterised by a rhythmic succession of siltstones, clays, fine-grained sandstones, marls, pelites bearing bivalves, siliceous chert nodules, and, to a lesser extent, oolitic carbonates. Although largely obscured by vegetation at present, representative outcrops of this formation are exposed in the Arroyo Vino area. The sedimentary structures within this unit are predominantly syngenetic in origin (Andreis *et al*., 1990).

3. Materials and methods

3.1 Materials: Herbst and Leguizamón (1984) reported that the fossil woods analysed in this study were collected during the late 1970s from the fossiliferous locality known as Arroyo Vino. The material belongs to the Dr Rafael Herbst Palaeontological Collection housed at the National University of the Northeast and is catalogued under the acronym CTES-PB 12337 (fragment I). The specimen is permanently deposited at the Centre for Applied Ecology of the Littoral (CECOAL–CONICET–UNNE), Corrientes, Argentina.

3.2 Methods: The fossil specimen was examined and documented using a combination of complementary analytical techniques, including X-ray micro-computed tomography (μCT), scanning electron microscopy coupled with energy-dispersive X-ray spectroscopy (SEM–EDS), and confocal Raman spectroscopy (CRS).

3.2.1 SEM–EDS: Scanning electron microscopy was performed using a Phenom ProX scanning electron microscope equipped with a backscattered electron detector and an energy-dispersive X-ray spectroscopy system (EDAX Genesis 2000) fitted with a Si(Li) detector and an ultra-thin polypropylene window. Analyses were carried out at the Bionanotechnology

Laboratory of NOA (INBIONATEC–CONICET–UNSE), Universidad Nacional de Santiago del Estero, Argentina. Analytical areas were carefully selected to avoid altered domains, targeting the flattest possible regions of the longitudinal section in order to minimise spurious X-ray generation from heterogeneous zones. The incident beam current, monitored using a Faraday cup, was set between 300 and 400 pA. A working distance of 15 mm was employed, corresponding to a 30° take-off angle for the EDS system, with an accelerating voltage of 15 keV. Under these conditions, the selected beam energy efficiently excited the characteristic X-ray lines of the constituent elements while limiting matrix effects and maintaining a relatively small interaction volume.

3.2.2 CRS: The specimen was analysed at the Bionanotechnology Laboratory of NOA (INBIONATEC–CONICET–UNSE) using a LabRAM HR Evolution (HORIBA) confocal Raman spectrometer, operated with excitation wavelengths of 532 nm and equipped with a 50× objective lens with a numerical aperture of 0.9. Measurements were acquired over a spectral range of 100–2500 cm^{-1}. The sample was mounted directly on a microscope slide without prior preparation. Analyses focused on the longitudinal section of the specimen, with the flattest areas selected to maximise signal intensity and capture chromatic variations. The acquired spectrum was subsequently processed using Origin software, applying baseline correction and noise reduction through convolution of Gaussian–Lorentzian (Voigt) functions.

3.2.3 MicroCT (μCT): Internal structural characterisation of the fossilised wood specimens was conducted via high-resolution X-ray micro-computed tomography (μCT) using a SkyScan 1273 system (Bruker MicroCT, Kontich, Belgium). This non-destructive technique is particularly efficacious for identifying petrological variations within permineralised tissues, as it facilitates the mapping of internal features based on the differential X-ray attenuation coefficients of various mineral phases.

Acquisition and Geometry: The system was operated at a voltage of 100 kV and a tube current of 166 μA, employing a 1.0 mm Al filter to harden the X-ray spectrum and mitigate artefacts arising from the high mineral density of the fossils. To ensure a comprehensive capture of the silicified or calcified anatomical structures, the geometry was optimised to achieve an isotropic voxel size of 10 μm (volumetric resolution: 1,000 μm^3). A full 360° rotations with a discrete step of 0.2° was employed, resulting in the acquisition of 1,800 radiographic projections. To ensure analytical transparency and reproducibility, the complete geochemical dataset and raw Raman spectra (Spot 04) have been deposited in a public repository (see Data Availability section; https://doi.org/10.5281/zenodo.18597970).

Image Reconstruction and Digital Petrography: The transition from raw radiographic projections to a volumetric dataset was achieved through a filtered back-projection algorithm using Bruker NRecon (v.1.8). During this phase, discretely sampled data fields were interpolated to approximate a continuous volumetric function. High-order interpolation schemes were utilised, ensuring that non-observed samples were accurately estimated via trilinear filtering to resolve complex three-dimensional textures and internal gradients (Kniss, 2002). In the context of fossil wood, the reconstructed 16-bit greyscale values serve as a proxy for relative density and atomic number (Z), enabling the discrimination between the primary mineralised lignocellulosic framework and secondary diagenetic infillings.

Segmentation and Mineral Phase Identification: Segmentation was executed to selectively isolate voxels representing specific mineralisations, thereby enhancing the analytical interpretability of the fossilised tissues. This procedure relied primarily on global and local

thresholding a robust approach that discriminates discrete mineral phases based on their X-ray attenuation intensity (Bankman, 2000). By isolating specific density ranges, user-defined three-dimensional models were generated to facilitate the precise evaluation of internal architectures (Sabella, 1988).

Following thresholding, the data underwent binarisation, transforming the continuous greyscale gradient into a logical binary mask. This step is critical for the subsequent quantification of permineralisation patterns, as it defines the precise boundaries of the mineralised framework (Chakkour, 2024). This non-destructive methodology allows for the precise mapping of internal structures based on variations in sample density and chemical composition (Machado *et al*., 2019).

Advanced Visualisation and Volumetric Analysis: For advanced structural differentiation, the reconstructed volumes were rendered using sophisticated colour-mapping techniques. Both RGB (red, green, blue) and HSV (hue, saturation, value) colour models were strategically employed to map density variations and spatial depth, allowing for the visual segregation of overlapping diagenetic components (Li *et al*., 2012). This "digital staining" facilitates the identification of distinct permineralisation pulses or vestigial organic structures that exhibit minute variations in X-ray attenuation, which would otherwise be indiscernible in a conventional monochrome display. Furthermore, the spatial position of each voxel remains implicitly defined by its location within the three-dimensional data array, ensuring the geometric integrity of the fossil wood model (Sutton, 2008; Vega *et al*., 2018).

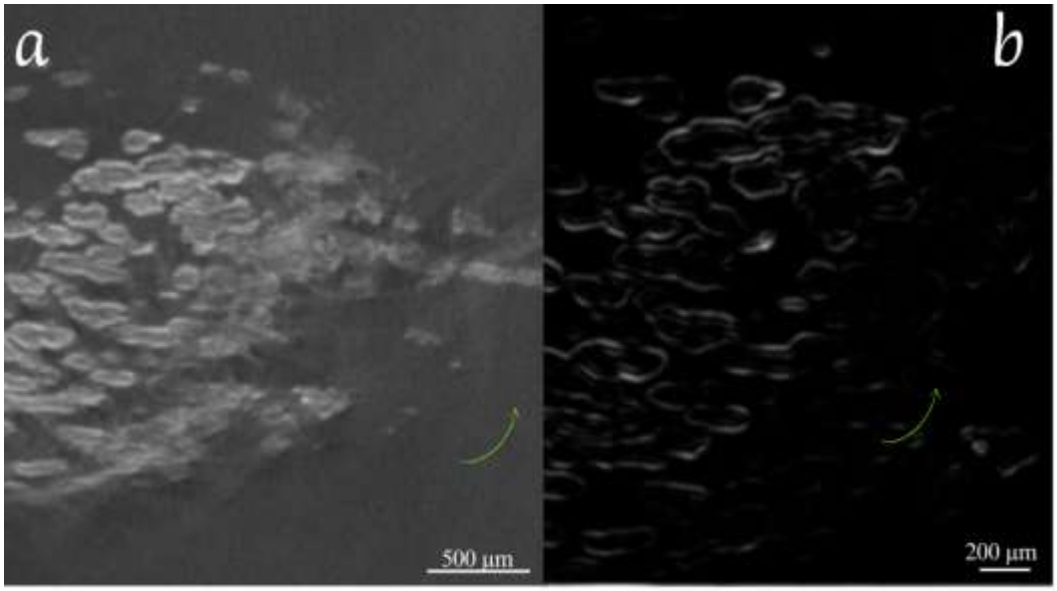
4. Results

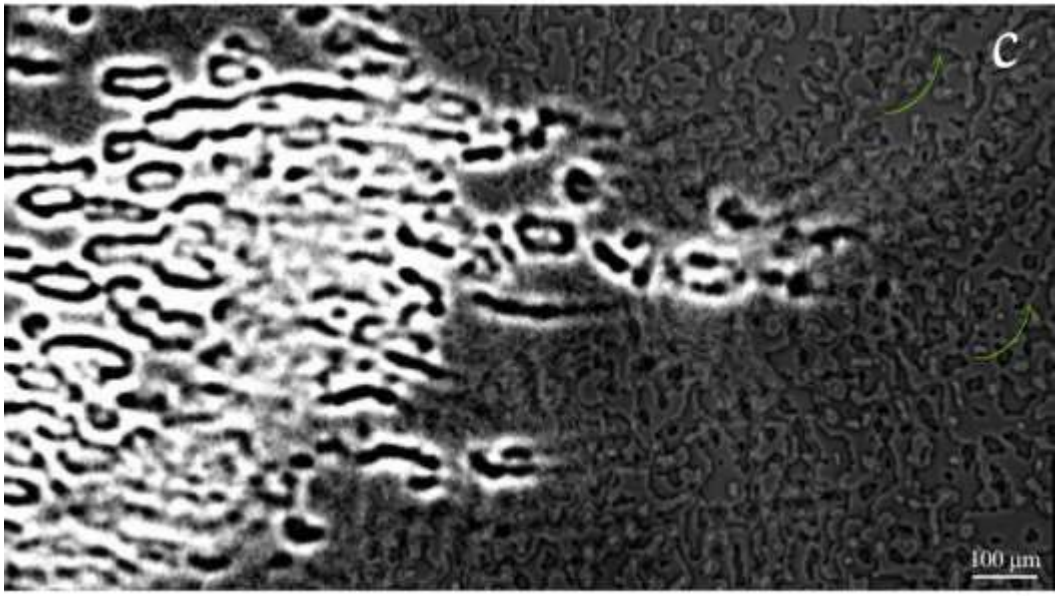
4.1 Thresholding and Segmentation Analysis

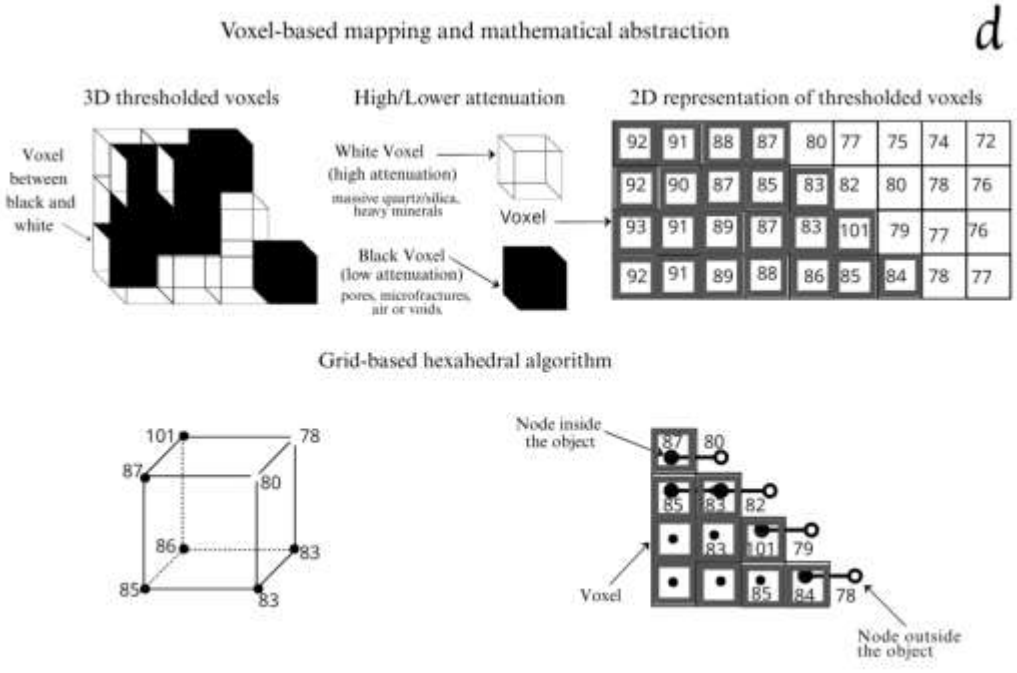
The volumetric analysis of the *Baieroxylon cicatricum* specimen yielded a processed volume of 1,200 mm^3, with a defined Region of Interest (ROI) encompassing a representative area of 100 mm^2. The application of high-resolution μCT to this taxon reveals a pronounced internal heterogeneity, characterised by distinct textural variations, exceptionally preserved cellular morphostructures, and a complex three-dimensional spatial distribution of mineral phases. In radiological and volumetric imaging, effective segmentation is contingent upon a rigorous preprocessing stage at the pixel and voxel level, designed to enhance structural and mineralogical discrimination. This systematic modification of individual values executed via a pixel-by-pixel scan in two-dimensional projections or a voxel-by-voxel scan within the three-dimensional dataset allows for precise attenuation filtering without compromising the integrity of adjacent elements.

The segmentation process was guided by statistical data extracted from the image histograms, which facilitated the identification of discrete grey-level populations. These populations correspond to the varying X-ray attenuation coefficients of the specimen's components, primarily differentiating the mineralised lignocellulosic framework from secondary diagenetic precipitates and the surrounding matrix (Gavidia *et al*., 2011; Li *et al*., 2024). Through the calibration of these greyscale thresholds, it was possible to isolate the tracheid walls of *B. cicatricum* from the inorganic infillings, providing a high-fidelity digital representation of the fossil's anatomy. The resulting binarised masks served as the foundation

for the volumetric quantification of permineralisation density and the spatial mapping of mineral gradients within the xylem.


a
500 µm
b
200 µm


c
100 µm


Voxel-based mapping and mathematical abstraction
d
3D thresholded voxels
High/Lower attenuation
2D representation of thresholded voxels
Voxel between black and white
White Voxel (high attenuation)
massive quartz/silica, heavy minerals
Voxel
Black Voxel (low attenuation)
pores, microfractures, air or voids
92 91 88 87 80 77 75 74 72
92 90 87 85 83 82 80 78 76
93 91 89 87 83 101 79 77 76
92 91 89 88 86 85 84 78 77
Grid-based hexahedral algorithm
101
78
87
80
86
83
85
83
Node inside the object
87 80
85 82
83 101 79
Voxel
85 84 78
Node outside the object

275

Figure 3. Methodological workflow for the digital petrography and volumetric segmentation of *Baieroxylon cicatricum*. (a) Raw μCT orthoslice illustrating initial X-ray attenuation gradients; scale bar = 500 μm. (b) Computationally enhanced section isolating high-attenuation tracheid boundaries from the lower-attenuation lumina; scale bar = 200 μm. (c) High-magnification micrograph highlighting cellular preservation; the 100 μm scale bar confirms the system's ability to resolve cell wall thicknesses at sub-10 μm levels. (d) Voxel-based mapping and mathematical abstraction. The schematics illustrate the 3D and 2D thresholding logic on a uniform hexahedral grid, where nodes situated at the barycentre of each voxel facilitate the transition to finite element analysis. Green arrows in (a), (b), and (c) denote the radial orientation of the xylem growth rings.

4.1.1 Analysis of Figure 3

Morphometric Resolution and Voxel Calibration: Following The spatial calibration of the *Baieroxylon cicatricum* datasets was rigorously maintained at an isotropic voxel size of 10 μm, ensuring high-fidelity morphometric analysis. As demonstrated in the methodological workflow (Figure 3), the primary orthoslices (Fig. 3a) provide a macroscopic overview of the silicified xylem, where the radial orientation of the growth rings remains clearly discernible (Lozano Gutiérrez *et al.*, 2018). Following Schneider's (1996) protocol, a representative sub-volume of the Region of Interest (ROI) was extracted for three-dimensional segmentation.

The segmentation logic was underpinned by an iterative thresholding analysis. Whilst an initial tentative threshold of 82 was evaluated (Carlson *et al.*, 2003; Chakkour, 2024), the definitive characterisation was achieved at a greyscale threshold of 84 (Fig. 3c). At this specific level, the cellular architecture and the spatial distribution of mineral phases reached optimal contrast, revealing a highly complex texture with distinct density gradients. Morphometric measurements at this threshold indicate an average cell wall thickness of approximately 9–10 μm, showing a robust correlation with the ultrastructural data obtained via Scanning Electron Microscopy (SEM) (Fig. 7c).

Volumetric Mapping and Attenuation Physics

The voxel-based intensity mapping (Fig. 3d) reveals the profound diagenetic heterogeneity of the specimen. In these 16-bit datasets (ranging from 0 to 65,535 greys), greyscale values act as a direct proxy for material density within the scanned volume (Du Plessis *et al.*, 2016). Although the mineralised tracheid walls typically align with the 84-threshold, localised clusters of high-attenuation mineral precipitates reach intensity values of 101. These 'bright spots' signify late-stage authigenic mineralisation pulses (Drebin *et al.*, 1987; Bennett *et al.*, 2013).

Data processing in this context is inherently complex; as the polychromatic X-ray source produces attenuation coefficients dependent on the source-detector coupling, voxel values may overlap even between mineralogically distinct phases (Du Plessis *et al.*, 2016; Machado *et al.*, 2019). Nevertheless, by refining the thresholding beyond the dark-voxel bias observed at higher levels (e.g., 90), this study provides a precise characterisation of wood petrification across scales ranging from the millimetric to the micronised, successfully segregating the botanical framework from the inorganic diagenetic matrix.

4.2 Three-Dimensional Volume Rendering and Mineral Phase Interpretation

The volumetric rendering of *Baieroxylon cicatricum* was executed using a combination of RGB and HSV mapping, facilitating the spectral discrimination of distinct mineral phases within the silicified matrix (Collinson *et al.*, 2016; Li *et al.*, 2024). By manipulating the transfer

functions and opacity gradients, it was possible to visualise the complex paragenetic sequence of the specimen in three dimensions (Figure 4).

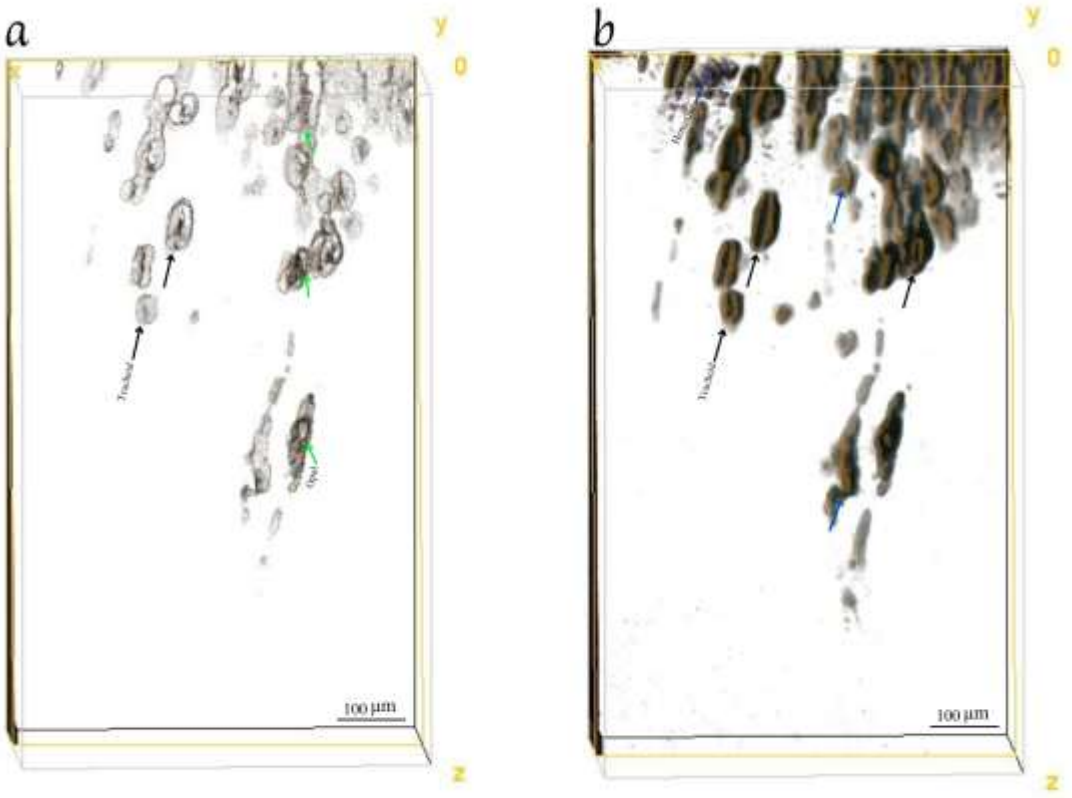


Figure 4. High-resolution 3D volumetric rendering of Baieroxylon cicatricum showcasing mineral-phase heterogeneity. (a) Isosurface reconstruction highlighting silicified tracheid walls (translucent brown) and spherulitic opal formations (semi-transparent) occluding the lumina. (b) Distribution of late-stage hematite (high-attenuation reddish-brown) within the elongated tracheid network. (c) Multi-mineralogical mapping: chalcedony (semi-transparent grey), crystalline quartz (translucent amber), and fossilised tracheidal framework (solid brown). (d) Longitudinal radial section displaying homogeneous mineralisation and post-mortem crystallisation patterns (striations) along the vascular fibres. Scale bars = 100 μm (calibrated to a 10 μm isotropic voxel size).

4.2.1 Analysis of Figure 4

Diagenetic Architecture and Mineral Polymorphs The 3D reconstructions, obtained via filtered back-projection (Bennett *et al.*, 2013), reveal that the secondary xylem has undergone extensive, multi-phasic permineralisation (Carlson *et al.*, 2003; Ensikat *et al.*, 2023). The μCT datasets identify a predominant silicification front, where metastable silica (opal) is preferentially arranged as a micro-intergrowth with crystalline quartz within the tracheid cell walls and parenchyma (Fig. 4a). The orientation of these polymorphic silica formations along the longitudinal z-axis indicates a diagenetic trend towards subsequent recrystallisation (Yu *et al.*, 2024).

As shown in Figure 4b, iron oxides (identified as hematite clusters) exhibit co-crystallisation with the quartz matrix. The remarkable definition of these internal morphostructures suggests a highly efficient fossilisation process, wherein mineral precipitation occurred rapidly enough to preclude significant cellular collapse (Nowak *et al.*, 2005). This high-fidelity preservation is further evidenced in Figure 4c, where the interplay of shadowing and highlights discriminates between high-density mineralised regions and low-density domains, the latter potentially representing residual organic matter or microscopic voids (Kniss, 2002; Géraud *et al.*, 2003).

The longitudinal sections (Fig. 4d) display a more homogenous mineral texture characterised by distinct striations, following the original orientation of the xylem fibres. These patterns reflect a high degree of post-mortem crystallisation, where mineral fluids exploited the primary vascular pathways (Collinson *et al.*, 2016). The observed polyphasic differences ranging from the granular, less organised textures in Fig. 4c to the complete mineral replacement in Fig. 4d confirm a sophisticated permineralisation history consistent with late-stage authigenic mineral pulses (Masschaele *et al.*, 2007; Drebin *et al.*, 1987).

4.3 Volume Rendering with Spectral Colours

The application of spectral pseudo-colouring provided an advanced diagnostic tool for discriminating between overlapping mineral phases within the *Baieroxylon cicatricum* xylem. By assigning specific colour channels to discrete X-ray attenuation spectra, it was possible to numerically evaluate the spatial regularisation of the reconstructed volumes (Salehjahromi *et al.*, 2018; Feng, 2022).

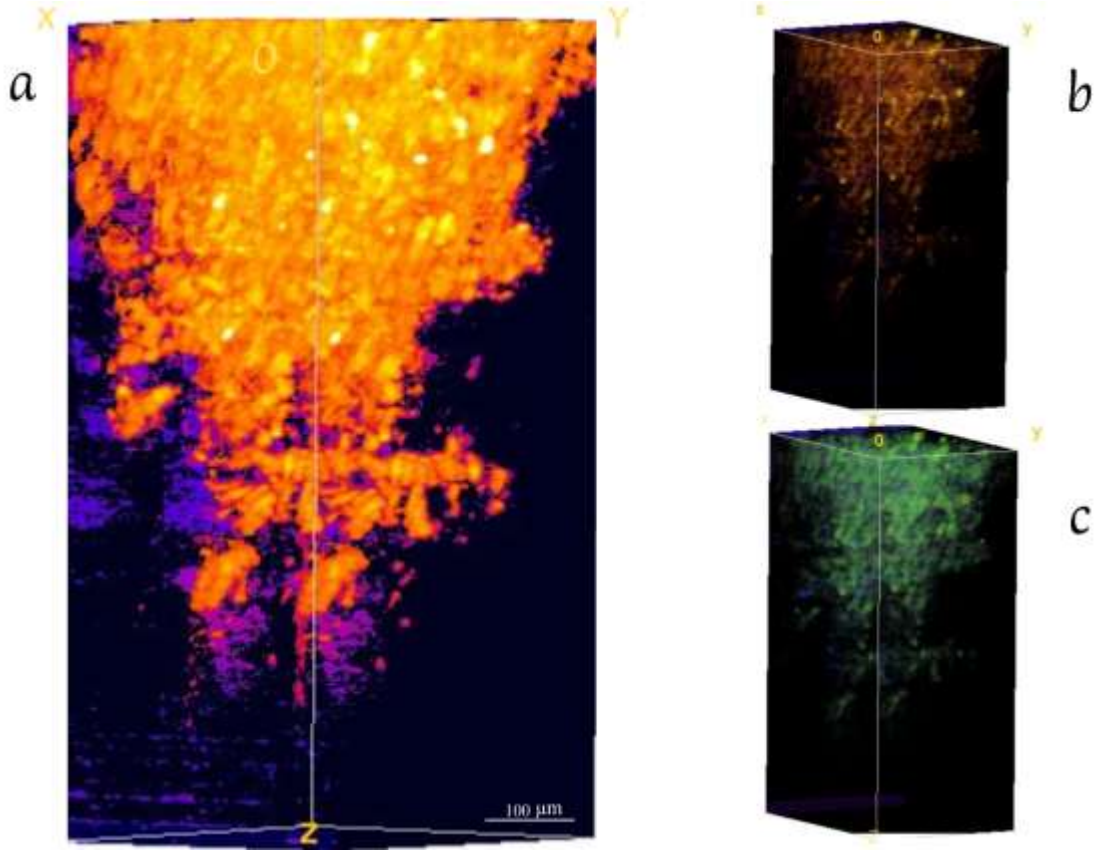


Figure 5. Spectral volume images of *Baieroxylon cicatricum* illustrating density-dependent mineralisation. (a) Pseudo-coloured orthoslice displaying high-density silica phases (orange/yellow) and low-density vestigial organic remnants (purple); hematite inclusions appear as high-attenuation white micro-clusters. (b) 3D volumetric cross-section highlighting the contrast between the silicified matrix (dark brown) and late-stage hematite precipitates (gold). (c) High-definition green-channel rendering used to accentuate anatomical textures and internal morphostructural variations. Scale bar = 100 μm.

4.3.1 Analysis of Figure 5

Multi-spectral Attenuation Patterns The spectral rendering (Figure 5a) utilises a dual-polarity colour ramp to segment density domains. Warm-spectrum colours (orange to bright yellow) identify high-density authigenic mineralisation, such as quartz and silica polymorphs, which were subsequently validated via Confocal Raman and SEM-EDS (Fig. 7c, d). Conversely, cool-spectrum colours (blue to bright purple) delineate lower-density regions, indicating vestigial organic matter or microporosity (Géraud *et al.*, 2003; Li *et al.*, 2024).

As illustrated in Figure 5b, the high-density hematite inclusions are rendered with gold-like hues, revealing their preferential occlusion of the tracheid lumina and their alignment along the z-axis (Nowak *et al.*, 2005; Salehjahromi *et al.*, 2017). This spatial distribution indicates that iron-rich mineralising pulses permeated the secondary xylem following silicification. The high-contrast green-channel rendering (Figure 5c) was strategically employed to highlight the micromorphological texture of the cellular tissue, revealing fine anatomical details that correlate with scanning-induced variations in mineral density (Ketcham and Carlson, 2001; Wang *et al.*, 2016).

4.4 Quantitative Voxel-Based Petrography and Multi-Phase Discrimination

The integration of advanced imaging techniques facilitates the acquisition of bulk density and effective atomic number (Zeff) mapping, a process fundamentally governed by the interplay between the photoelectric effect and Compton scattering (Vinegar, 1986). In this study, the Region of Interest (ROI) was subjected to a false-colour polyphasic segmentation to discriminate between complex mineral assemblages within the *Baieroxylon cicatricum* framework (Figure 6).

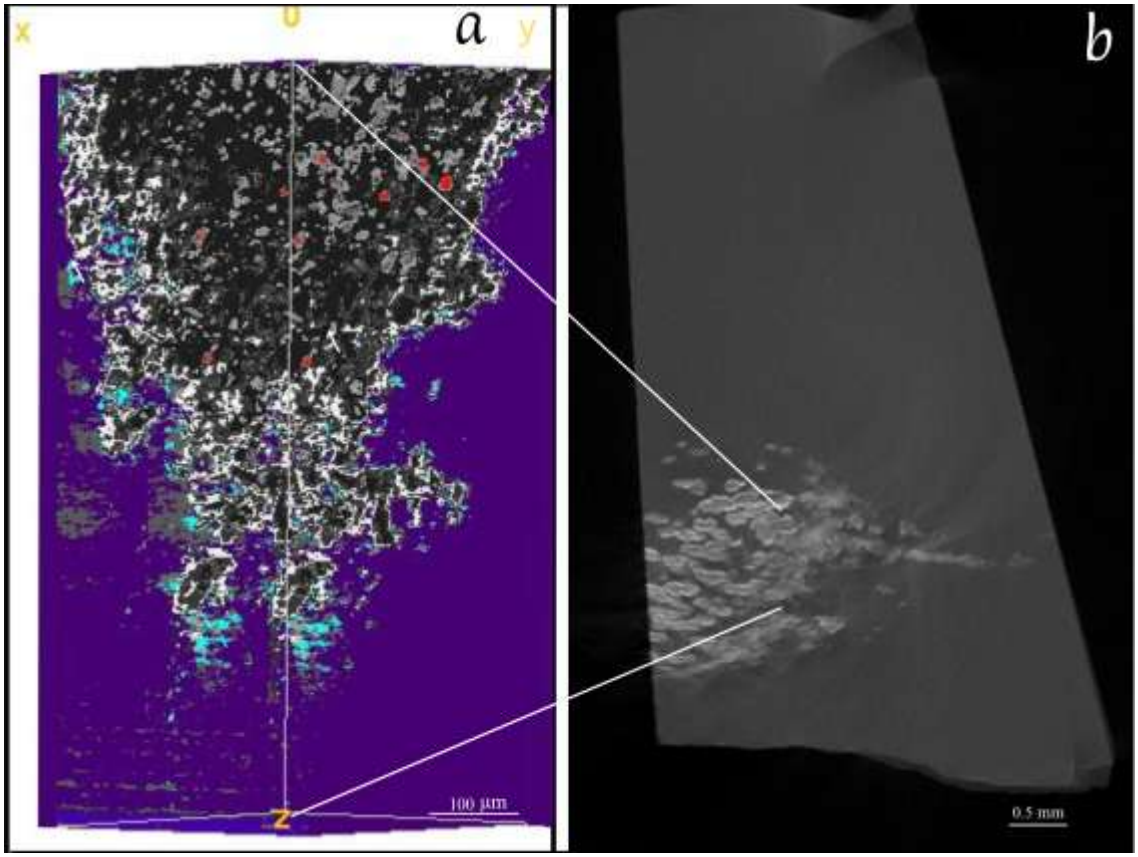


Figure 6. Digital petrographic characterisation and ROI segmentation of *Baieroxylon cicatricum*. (a) Volumetric false-colour rendering displaying polyphasic mineral distribution (quartz: black; hematite: red; silica polymorphs: white; calcite: light blue). Colour assignments are calibrated against X-ray attenuation coefficients and validated via SEM-EDS. Scale bar = 100 μm. (b) Raw μCT cross-section highlighting the original ROI; the high-contrast greyscale indicates the preservation of tracheidal and parenchymatous structures. Scale bar = 0.5 mm.

4.4.1 Analysis of Figure 6

Mineralogical Mapping and Structural Preservation The false-colour volumetric reconstruction (Fig. 6a) serves as a digital proxy for the internal geochemical heterogeneity, where RGB band modifications were strategically employed to isolate zones of varying mineral composition (Ketcham and Carlson, 2001; Li *et al.*, 2024). These μCT data were rigorously cross-validated using Confocal Raman spectroscopy (Fig. 8) and SEM-EDS to ensure phase-identification accuracy (Kniss, 2002): High-Density Domains (black, correlate with crystalline quartz matrices). Very High-Density Phases (red, represent disseminated hematite clusters). Medium-Density Phases (light grey/white, correspond to clay minerals and silica polymorphs).

Low-Density/Porous Domains (Light blue/purple, identify calcite infillings or primary void spaces within the lignocellulosic framework) (Pakhnevich *et al.*, 2024).

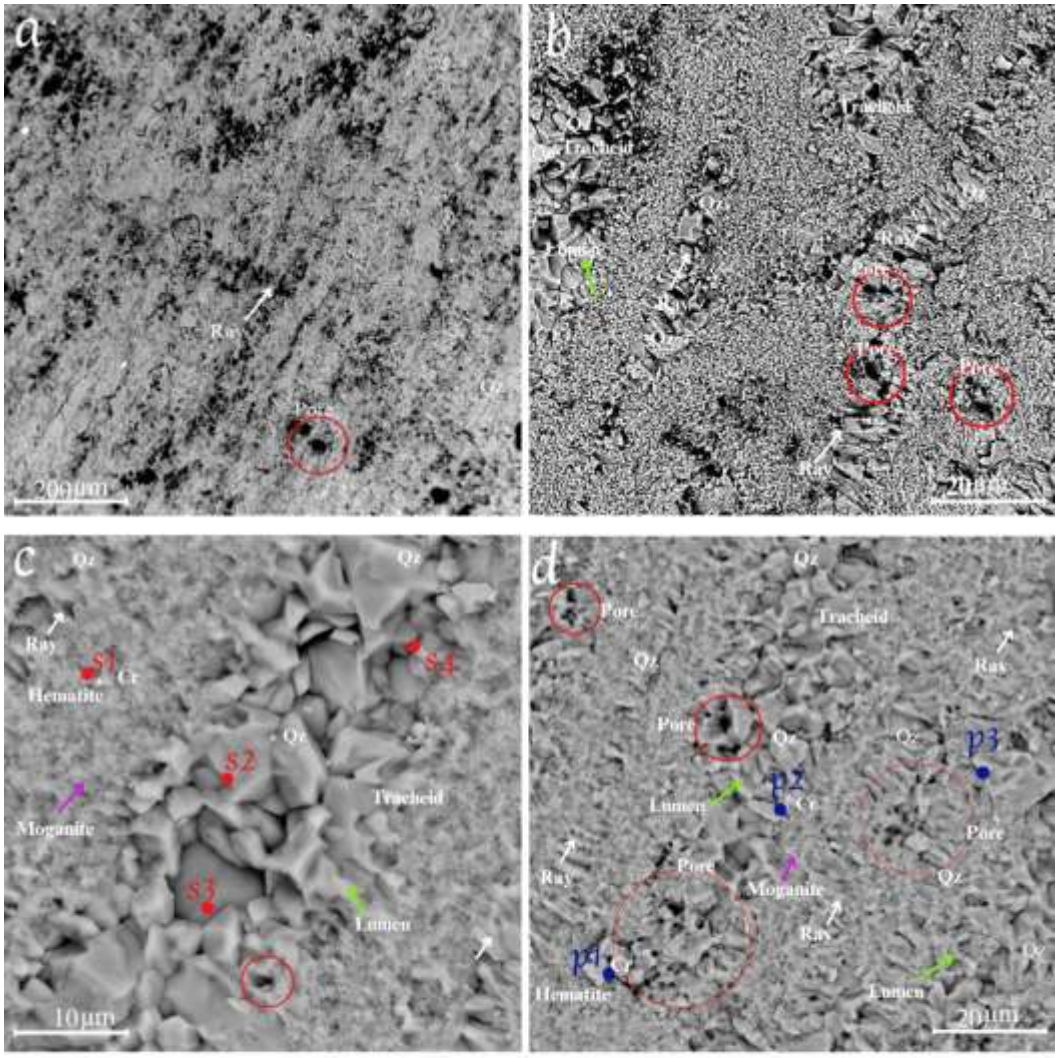
The original orthoslices (Fig. 6b) exhibit a high-fidelity representation of the internal anatomy, characterised by three distinct attenuation phases (dark grey, light grey, and bright white). The preservation of granular and elongated crystallographic textures, alongside the sharp definition of tracheids and parenchyma, confirms the exceptional taphonomic quality of the specimen (Staedler *et al.*, 2013; Gee, 2013). This level of detail suggests that the mineralisation process was sufficiently rapid to encapsulate the wood's micro-architecture before diagenetic distortion occurred.

4.5 Synergistic Validation: SEM-BSE-EDS and Digital Petrography

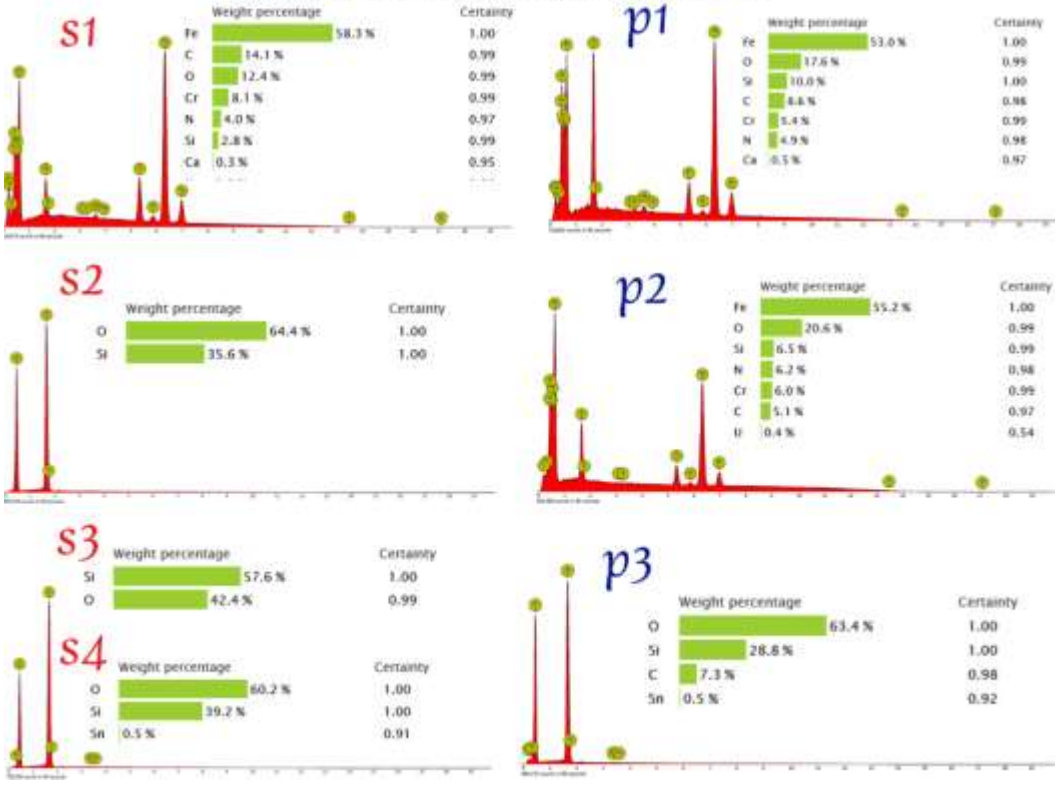
To corroborate the mineral phases identified via μCT attenuation gradients, a complementary ultrastructural and geochemical analysis was conducted using Scanning Electron Microscopy (SEM) in Backscattered Electron (BSE) mode, coupled with Energy Dispersive X-ray Spectroscopy (EDS). This multi-analytical approach facilitates the direct correlation between volumetric greyscale populations and the elemental composition of the mineral matrix (Ali *et al.*, 2023).

Table 1. Elemental composition (EDS) of the permineralised *B. cicatricum* specimen.

Location	Fe (%)	O (%)	Si (%)	C (%)	Trace Elements / Others (%)
s1	58.3	12.4	2.8	14.1	Cr (8.1), N (4.0), Ca (0.3)
p1	53.0	17.6	10.0	8.6	Cr (5.4), N (4.9), Ca (0.5)
p2	55.2	20.6	6.5	5.1	Cr (6.0), N (6.2), U (0.4)
p3	-	63.4	28.8	7.3	Sn (0.5)



Semiquantitative EDS analysis at the points in Figure



465

Figure 7. Ultrastructural and geochemical characterisation of *Baieroxylon cicatricum* via SEM-BSE and EDS. (a) Low-magnification BSE micrograph of the tangential section, illustrating the high-fidelity preservation of the xylem texture and multiseriate rays (white arrow). (b) Detailed view of the radial section; the secondary xylem is entirely permineralised, with subhedral quartz crystals (Qz) prograding into the tracheid lumina and ray parenchyma. (c-d) High-magnification micrographs highlighting the co-occurrence of α-quartz and microcrystalline moganite (purple arrow) within the mineralised framework. Red and blue loci (s1–s4 and p1–p3) denote the specific points of semi-quantitative EDS analysis. (Lower panels) representative EDS spectra and elemental weight percentages corresponding to the identified loci. Note the high iron (Fe) concentrations in high-attenuation clusters (s1, p1, p2) and the dominance of silica (Si/O) in the primary structural matrix. Scale bars: (a) 200 μm, (b, d) 20 μm, (c) 10 μm.

4.5.1 Analysis of Figure 7: Ultrastructural Characterisation

In the The BSE micrographs (Fig. 7a, b) provide a high-resolution view of the secondary xylem, where the contrast is a direct function of the mean atomic number (Z). The secondary xylem of *Baieroxylon cicatricum* exhibits exceptional permineralisation fidelity; well-developed subhedral quartz crystals, reaching lengths of up to ~10 μm, are observed emanating from interfacial matrix regions and prograding towards the centre of the tracheid lumina and ray parenchyma (Fig. 7c, d). According to Çevik Üner *et al.* (2022), this dense, homogenous texture is indicative of complete petrification. The analysis reveals a complex siliceous assemblage comprising micrometric chalcedonic quartz within the secondary xylem, alongside subcrystalline moganite and submicrometric opal dispersed throughout the surrounding matrix (Fig. 7c, d). These findings validate the "intermediate" attenuation values (threshold 84) observed in the μCT segmentations as polymorphic silica phases.

Geochemical Mapping and Trace Element Analysis (Table 1).

Semi-quantitative EDS analysis (Table 1) identifies Fe, O, and Si as the predominant elements, confirming the prevalence of silicification and the presence of iron-rich authigenic clusters.

High-Attenuation Phases (Iron oxides): Locations s1, p1, and p2 exhibit high iron concentrations (averaging 55.5% Fe), validating the "bright spots" (intensity value 101) identified in the volumetric rendering as hematite or related iron oxides.

Siliceous Framework: Locations s2, s3, s4, and p3 show a clear dominance of Si and O, corresponding to the α-quartz and moganite phases that constitute the petrified plant structure.

Residual Organic Matter: The detection of minor carbon peaks (averaging 9% C in specific loci) suggests the preservation of vestigial organic relicts within the less mineralised domains, providing a biological anchor for the mineral matrix.

Palaeoenvironmental Implications: The consistent presence of chromium (Cr), averaging 7.56% in iron-rich zones, is particularly noteworthy (see the Geochemical_Analytical_Data folder, Supplementary Tables S1 and S2, in the Zenodo repository for the complete elemental quantification). This suggests that the mineralising fluids originated from a local fault zone within the tectosedimentary basin of Guairá. The hydrogeological conditions south of the Tebicuary-mí River facilitated the concentration of transition elements (Fe, Cr) and trace elements (Sn, U), which infiltrated the wood during the early stages of burial, resulting in the unique spectral attenuation patterns captured by the μCT (Fig. 7).

4.6 Molecular Validation via Confocal Raman Spectroscopy (CRS)

To achieve a comprehensive characterisation of the petrification fabric, Confocal Raman Spectroscopy (CRS) was employed to identify the crystalline and amorphous phases at sub-micrometric scales. This technique, founded on the inelastic scattering of monochromatic light (Raman, 1928), allows for the discrimination of silica polymorphs that are otherwise indistinguishable by density alone. The use of a confocal setup effectively eliminated parasitic

backgrounds, ensuring a high signal-to-noise ratio for the detection of thin mineral coatings and intergrowths (Dieing *et al.*, 2011; Frezzotti *et al.*, 2012).

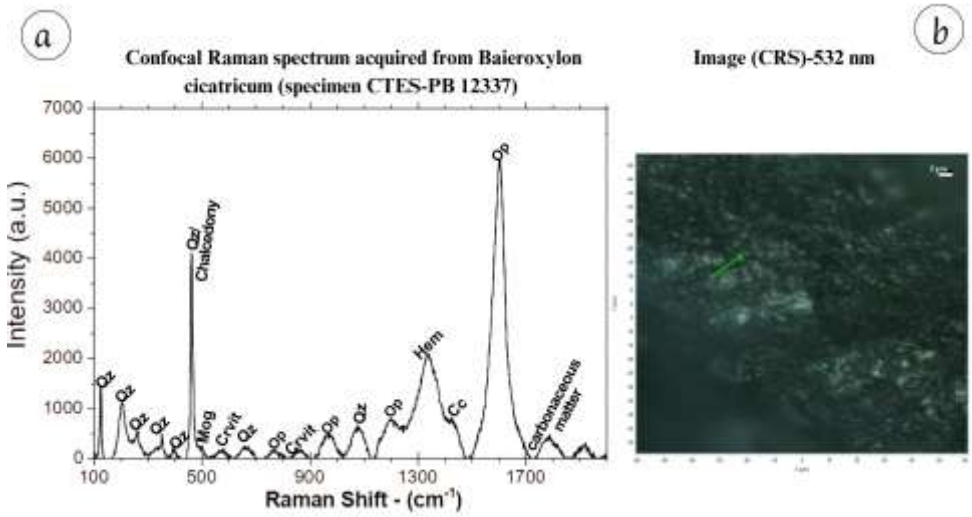


Figure 8. Confocal Raman Spectroscopy (CRS) validation of the *Baieroxylon cicatricum* mineral matrix. (a) Representative Raman spectrum illustrating the molecular diversity of the specimen. Essential vibrational modes include: Qz/Chalcedony (quartz lattice); Mog (moganite); Op (opal intergrowths); Hem (hematite); Cc (calcite); and Crvit (uvarovite/chromium-rich phases). The presence of carbonaceous matter at high Raman shifts confirms vestigial organic preservation. (b) Confocal micrograph (532 nm excitation) showing the target area within the tracheid-ray interface; the green crosshair denotes the point of spectral acquisition. Scale bar = 5 μm.

4.6.1 Spectral Analysis and Polymorphic Discrimination (Figure 8)

The vibrational spectra (Fig. 8) confirm that the secondary xylem of *B. cicatricum* is a complex mineralogical mosaic. The dominant siliceous matrix is composed of alpha-quartz and chalcedony, identified by the intense primary vibrational mode at 464 cm^{-1} and the characteristic lattice modes at 128, 206, and 402 cm^{-1}.

Significantly, the presence of monoclinic moganite was detected at 503 cm^{-1}. As moganite is a metastable silica polymorph, its preservation within the quartz matrix provides significant insight into the diagenetic maturity of the specimen. Furthermore, the opal phases previously identified via μCT as low-attenuation infillings (Fig. 3a) were molecularly confirmed by broad bands at 787, 978, and the exceptionally intense mode at 1587 cm^{-1}.

Secondary Mineral Inclusions: Beyond the siliceous framework, CRS resolved the late-stage precipitates that contribute to the high-attenuation clusters observed in the μCT volume renderings: Hematite: Resolved at 1313 cm^{-1}, validating the high-attenuation clusters identified in the 3D voxel maps. Calcite: Identified at 1435 cm^{-1}, corresponding to the low-density interstitial infillings. Uvarovite (Chromium-garnet): Detected at 590 and 894 cm^{-1}, providing a mineralogical context for the high chromium (Cr) concentrations recorded by EDS. Carbonaceous Matter: Raman shifts above 1700 cm^{-1} indicate the presence of disordered organic relicts, suggesting that the permineralisation process encapsulated primary biological molecules (Pakhnevich *et al.*, 2024).

4.6.2 Integrated Model of Sequential Mineralisation

The synergy between 3D μCT rendering and Confocal Raman Imaging reveals a sophisticated, multi-stage paragenetic sequence. While traditional models might suggest a simple, epigenetic silification, the spatial distribution of opal found disseminated within 3D quartz networks rather than enclosed within cell walls (Fig. 4a) implies that its deposition postdates the initial petrification.

This suggests that *B. cicatricum* underwent a primary silification event that stabilised the cellular morphostructure, followed by a secondary infiltration of silica-rich metasomatic fluids at a more recent geological time (Mustoe, 2023; Gee, 2013). The transition from "warm" to "cool" spectral tones in our volumetric models (Fig. 5) thus reflects not just density, but the temporal evolution of the fossil: from the stable quartz framework to late-stage authigenic pulses of iron oxides and amorphous silica polymorphs (Ensikat *et al.*, 2023).

5. Discussion

5.1 Taphonomic Implications of μCT Attenuation and Voxel Fidelity

The application of high-resolution μCT to *Baieroxylon cicatricum* demonstrates that X-ray attenuation is not merely a function of visual contrast, but a precise proxy for the volumetric substitution of woody tissues by mineralising fluids. The results indicate that the petrification process followed a strict volume-by-volume replacement model. The isotropic voxel resolution of 10 μm permitted the identification of crystallographic textures with a sharpness that surpasses conventional petrographic thin sections, particularly within the designated Region of Interest (ROI).

5.2 Paragenetic Sequence: From Initial Silification to Late-Stage Pulses

The synergy between μCT, SEM-BSE-EDS, and Confocal Raman Spectroscopy (CRS) reveals that mineralisation occurred in two distinct, sophisticated episodes:
Primary Episode (Upper Permian Lithification): Initial infiltration by silica-rich fluids led to the permineralisation of the cell walls. This stage is characterised by the transition to stable α-quartz and the co-precipitation of hematite, which accounts for the high-attenuation clusters (intensity 101) identified in the volumetric mapping.
Secondary Episode (Metasomatic Infiltration): A subsequent event introduced metastable silica polymorphs, specifically moganite and opal, into the remaining void spaces and fractures.
The detection of opal is particularly significant. While Mustoe (2023) suggests that opal-A is typically restricted to Neogene formations, its presence in *B. cicatricum* spatially disseminated within 3D quartz networks rather than enclosed within cell walls supports a model of late-stage metasomatic contribution. This indicates that the fossil remained permeable to mineralising fluids long after the primary burial, coinciding with findings by Yu *et al*. (2024) regarding opal precipitation in Permian woods.

5.3 Geochemical Heterogeneity and Palaeoenvironmental Context

The polyphasic mineralogy, ranging from megacryptocrystalline quartz to trace transition elements, reflects a complex tectosedimentary setting. The presence of chromium (Cr), averaging 7.56%, suggests that the mineralising fluids were influenced by local fault zones south of the Tebicuary-mí River, facilitating the concentration of transition elements during diagenesis.

Furthermore, the weak carbon signals detected via EDS (averaging 9% C) in less mineralised domains confirm the preservation of vestigial organic relicts. This biological anchor, encapsulated within a heterogeneous mineral matrix of varying X-ray absorption

coefficients, represents a significant advance in the understanding of Permian palaeoclimates. By integrating 16-bit μCT data with molecular spectroscopy, the present study builds upon and incorporates comparative studies on palaeobotanical morphostructures, composition, and mineralogy conducted by Wellington and Vinegar (1987), Carlson *et al*. (2003), Nowak *et al*. (2005), Lozano Gutiérrez *et al*. (2018), Ensikat *et al*. (2023), and Pakhnevich *et al*. (2024).

5.4 Integrated Palaeontological Inferences

5.4.1 Palaeoclimatic Considerations

The integrated analysis of the specimen, particularly the elevated concentrations of hematite identified through μCT and corroborated by EDS (Table 1), suggests that these Ginkgoales developed under a predominantly warm climatic regime. The markedly low levels of calcite and the scarcity of carbonate-forming elements detected across the vibrational spectra (Figs. 7 and 8) point to sustained humid conditions capable of supporting continuous and stable arboreal growth (Baez *et al*., 2025). Taken together, these lines of evidence are consistent with the established Permian palaeofloral records of Paraguay, which indicate the presence of gymnosperm-dominated forested landscapes under humid, thermophilic conditions. Rather than driving anatomical complexity, this palaeoenvironmental context likely favoured the persistence and ecological expansion of woody plants with fully developed vascular systems, in agreement with the regional framework proposed for the Late Permian (Bernstein and Waychunas, 1987; Crisafulli and Herbst, 2009).

5.4.2 Palaeoenvironmental and Diagenetic Dynamics

From a regional perspective, the study area forms part of a complex tectosedimentary basin whose evolution was controlled by subsidence, structural reorganisation, and fluid circulation. The limited calcite mineralisation and the minor occurrence of amorphous silica observed in the volumetric renderings (Figs. 4 and 6) are consistent with a predominantly continental system, most likely dominated by fluvial and lacustrine conditions during the Permian. Within this framework, regional tectonic dynamics would have favoured the establishment of warm and humid environments in the Tacuary Formation of the Guaireña Basin (Fúlfaro, 1996; Presser *et al*., 2000; Baez *et al*., 2024).

Compositionally, the xylem of *Baieroxylon cicatricum* is dominated by Fe, Si, and O, together with subcrystalline silica phases, including micrometric opal microspheres identified in the 3D models (Fig. 4). The heterogeneous spatial distribution of these components suggests a polyphasic diagenetic history linked to successive pulses of mineralising fluids. The presence of transition elements such as Cr, U, and Sn points to geochemical mobilisation associated with structurally controlled pathways (Table 1). Furthermore, the detection of residual carbonaceous matter (up to 14.1 wt%) indicates the preservation of lignin-derived relicts, confirming that silica replacement was highly efficient and enabled the early encapsulation of primary biological tissues (Mustoe, 2017; Ensikat *et al*., 2023; Pakhnevich *et al*., 2024).

5.4.3 Palaeobiogeographical Significance

During the Permian, eastern Paraguay formed part of the western margin of the Paraná intracratonic basin within the Gondwanan supercontinent (Báez Presser, 2012). The mineralisation patterns observed in the specimen, dominated by quartz and iron oxides, reflect the influence of the regional tectosedimentary framework on silicification and preservation processes. The occurrence of *Baieroxylon cicatricum* in the Guairá region allows comparisons with other Permian assemblages across southern South America. In particular, the deposits of the Tacuary Formation show lithological and palaeobotanical affinities with the Permian Yaguarí Formation of Uruguay, while floristic similarities with Triassic assemblages, such as those documented in the Tiki Formation of India, suggest the continuity and dispersal of

Ginkgoalean lineages across the Palaeozoic–Mesozoic boundary. Taken together, these correspondences are consistent with a broad Gondwanan distribution of these gymnosperms during this interval (Crisafulli and Herbst, 2009).

6. Conclusion

The multi-analytical investigation of *Baieroxylon cicatricum* from the Permian of Paraguay represents a significant methodological advancement in the study of silicified fossil woods. By integrating high-resolution X-ray micro-computed tomography (μCT) with SEM-BSE-EDS and Confocal Raman Spectroscopy (CRS), this study provides an unprecedented three-dimensional characterisation of the petrification fabric.

The primary contribution of this research lies in the successful application of Digital Petrography to resolve anatomical and mineralogical complexities at an isotropic voxel size of 10 μm. The μCT volume renderings, calibrated against 16-bit attenuation gradients, revealed a highly heterogeneous diagenetic history. The identification of stable α-quartz and hematite as the primary mineralising phases, followed by late-stage metasomatic pulses of moganite and opal, challenges the traditional view of single-event permineralisation. The spatial dissemination of opal within the 3D quartz framework molecularly validated by CRS suggests that the fossil remained geochemically active long after the initial lithification.

Furthermore, the detection of transition elements such as chromium (7.56%) and uranium, alongside preserved carbonaceous matter (14.1%), provides a robust geochemical proxy for the palaeoenvironmental conditions of the Guaireña Basin. These findings confirm that the fossilisation process occurred in a warm, humid continental environment influenced by active tectonic faulting at the western margin of the Gondwanan Paraná Basin.

In conclusion, the synergy of these advanced non-destructive and micro-analytical techniques facilitates a transition from descriptive palaeoxylology to Quantitative Digital Tapho-geochemistry. This study not only clarifies the taxonomic and palaeobiogeographical position of *B. cicatricum* within the Upper Permian floras of South America, but also establishes a new diagnostic benchmark for interpreting complex mineralisation sequences in the fossil record.

Funding: This research received no external funding.

Data Availability: The datasets generated and analysed during the current study are available in the Zenodo repository at https://doi.org/10.5281/zenodo.18597970. This repository includes: High-resolution micro-CT data: 1428 original slices and a priority subset of 114 ROI slices in TIFF format. 3D Visualisation: An animated fly-through (GIF) illustrating the spatial distribution of mineral inclusions. Geochemical validation: Table S1 (Raman peak assignments for silica polymorphs) and Table S2 (SEM-EDS elemental quantification, including Cr, Fe, and U concentrations). Analytical raw data: Original ASCII spectra for Raman Spot 04. All data are provided under a Creative Commons Attribution 4.0 International (CC BY 4.0) licence, ensuring full transparency and reproducibility of the taphonomic and geochemical interpretations presented in this work.

Acknowledgements

The authors express their sincere gratitude to the Agricultural Experimental Station of the National Institute of Agricultural Technology (EEA-INTA), Montecarlo, Misiones, Argentina, which, through Project BID 2853/OC-AR, enabled the acquisition of the X-ray microtomograph and supported the development of the research presented here. Special thanks are extended to the Director, María Elena Gauchat, and particularly to Dr Ángela Rosa Winck and Eng. Elsa Iris

Figueredo for their valuable assistance in the development and implementation of the applied methodologies. The authors also acknowledge the Skyscan/Instrutécnica team for providing essential technical training and foundational knowledge on the operation of the equipment and the associated techniques. This research was further supported by Project PI 2022/F 024, funded by the General Secretariat for Science and Technology of the National University of the Northeast, Argentina.

Conflicts of Interest: The authors declare no known competing financial interests or personal relationships that could have influenced the work reported in this paper.

References

Ali, A., Zhang, N., Santos, R. M. (2023). Mineral characterization using scanning electron microscopy (SEM): a review of the fundamentals, advancements, and research directions. *Applied Sciences*, *13*(23), 12600. https://doi.org/10.3390/app132312600.

Almeida, F.F.M. & Hasui, Y. (1984) O Pré-Cambriano do Brasil. Editora Edgard Blücher Ltda. São Paulo, 378p. https://www.estantevirtual.com.br/busca/o-pre-cambriano-do-brasil.

Andreis, R. R., Ferrando, L. A., Jalfin, G. A. (1990). Las secuencias del grupo independencia (permico) aflorantes en colinia independencia y al oeste de Caaguazú, Paraguay oriental: litofacies, paleocorrientes e interpretación paleoambiental. *Ciencia e Natura*, 29-34. https://doi.org/10.5902/2179460X26193.

Baez, E., Crisafulli, A. M. C., Kanbour, A. E., de los Ángeles Zuliani, P. (2024). Estudio mineralógico de maderas petrificadas de la Formación Carapacha (pérmico), La Pampa, Argentina. *FACENA*, *34*(1), 127-151. https://doi.org/10.30972/fac.3417555.

Baez, E., Crisafulli, A., Kanbour, A., Zuliani, P. (2025). Spectroscopic and SEM-EDS studies of gymnosperm wood from the Upper Permian Tacuary Formation, Paraguay. Journal of South American Earth Sciences 164: https://doi.org/10.1016/j.jsames.2025.105681.

Baez, E., Crisafulli, A., Kanbour, A., Bulman Hartkopf, C., Salinas Franco, N. D., López, D., & Gadea Villalba, M. A. (2026). *Dataset for the quantitative digital tapho-geochemistry of Baieroxylon cicatricum from the Permian of Paraguay*. Zenodo. https://doi.org/10.5281/zenodo.18597970.

Báez Presser, J. L. (2012). Distinción sismológica entre el manto Arqueozoico y el Proterozoico: la raíz de la litósfera bajo la cuenca del Paraná, América del Sur. https://revistascientificas.una.py/index.php/rcfacen/article/view/1043.

Bankman, I. (2000). *Handbook of medical imaging: processing and analysis management*. Academic press. https://shop.elsevier.com/books/handbook-of-medical-imaging/bankman/978-0-12-077790-7.

Bartrina, L. 2007 “Contexto geográfico general” en Salas Dueñas, D., y Facetti J.F. (Eds) 2007 Biodiversidad del Paraguay. Una aproximación a sus realidades (Asunción: Fundación Moisés Bertoni. USAID, GEF/BM. ISBN: 978-99953-48-00-7)

727 Barron, A. (2024). Applications of microCT imaging to archaeobotanical research. *Journal of*
728 *Archaeological Method and Theory*, *31*(2), 557-592. https://doi.org/10.1007/s10816-
729 023-09610-z.

730 Bennett, J. R., Opie, A. M., Xu, Q., Yu, H., Walsh, M., Butler, A., Bulter, P., Cao, G., Mohs,
731 A., Wang, G. (2013). Hybrid spectral micro-CT: system design, implementation, and
732 preliminary results. *IEEE transactions on biomedical engineering*, *61*(2), 246-253.
733 https://doi.org/10.1109/TBME.2013.2279673.

734 Bernstein, L. R., Waychunas, G. A. (1987). Germanium crystal chemistry in hematite and
735 goethite from the Apex Mine, Utah, and some new data on germanium in aqueous
736 solution and in stottite. *Geochimica et Cosmochimica Acta*, *51*(3), 623-630.
737 https://doi.org/10.1016/0016-7037(87)90074-3.

738 Calo, M., Rizzutto, M. A., Carmello-Guerreiro, S. M., Dias, C. S. B., Watling, J., Shock, M. P.,
739 Zimpel, C. A., Furquim, L. P., Pugliese, F., Neves, G. (2020). A correlation analysis of
740 Light Microscopy and X-ray Microct imaging methods applied to archaeological plant
741 remains' morphological attrib utes visualization.Scientific Reports, 10.
742 https://doi.org/10.1038/s41598-020-71726-z.

743 Carlson, W. D., Rowe, T., Ketcham, R. A., Colbert, M. W. (2003). Applications of high-
744 resolution X-ray computed tomography in petrology, meteoritics and palaeontology.
745 https://doi.org/10.1144/GSL.SP.2003.215.01.02.

746 Çevik Üner, B., Yılmaz Şahin, S., Akkemik, Ü. (2022). Mineralogical and palaeobotanical
747 investigations of Thrace Basin (NW Turkey). Turkish Journal of Earth Sciences.
748 Tübitak. https://doi.org/10.3906/yer-2106-2.

749 Chakkour, T. (2024). Finite element modelling of complex 3D image data with quantification
750 and analysis. *Oxford Open Materials Science*, *4*(1), itae003.
751 https://doi.org/10.1093/oxfmat/itae003.

752 Crisafulli, A. (2000). Maderas gimnospérmicas de Formación Independencia (Pérmico
753 Superior), Paraguay. XI Simposio Argentino de Paleobotánica y Palinología.
754 Resúmenes: 21.
755 https://www.ameghiniana.org.ar/index.php/ameghiniana/article/view/2565.

756 Crisafulli, A. (2001). Leños pérmicos de la Formación Yaguarí, República Oriental del
757 Uruguay. *Ameghiniana*, *38*(1), 61-72.
758 https://www.ameghiniana.org.ar/index.php/ameghiniana/article/view/2587.

759 Crisafulli, A. (2004). "Estudios xilotafoflorísticos en el Pérmico de Argentina, Paraguay y
760 Uruguay, con consideraciones paleoclimáticas y paleogeográficas". Tesis inédita.
761 FACENA-UNNE. 280 pp.
762 https://redbiblio.unne.edu.ar/pergamo/documento.php?ui=16&recno=77094&id=RESIS
763 TENCIA.16.77094.

764 Crisafulli, A., Herbst, R. (2009). Gymnospermous woods (Coniferales, Taxales, and
765 Ginkgoales) from the Upper Permian Tacuary Formation, Eastern Paraguay.
766 *Palaeobiodiversity and Palaeoenvironments*, *89*, 95-109.
767 https://doi.org/10.1007/s12549-009-005-5.

768 Collinson, M. E., Adams, N. F., Manchester, S. R., Stull, G. W., Herrera, F., Smith, S. Y.,
769 Andrew M, J., Kenrick, P., Sykes, D. (2016). X-ray micro-computed tomography
770 (micro-CT) of pyrite-permineralized fruits and seeds from the London Clay Formation
771 (Ypresian) conserved in silicone oil: a critical evaluation. *Botany*, *94*(9), 697-71 R. A.,
772 Carpenter, L., & Hanrahan, P. (1988). Volume rendering. *ACM Siggraph Computer*
773 *Graphics*, *22*(4), 65-74. https://doi.org/10.1139/cjb-2016-0078.

774 Dieing, T., Hollricher, O., Toporski, J. (Eds.). (2011). *Confocal raman microscopy* (Vol. 158).
775 Springer Science & Business Media. https://www.buscalibre.com.ar/libro-confocal-
776 raman-microscopy/9783030092177/p/57130201.

777 Drebin, R. A., Fishman, E. K., & Magid, D. (1987). Volumetric three-dimensional image
778 rendering: Thresholding versus nonthresholding techniques. In *Radiological Society of*
779 *North America 73rd scientific assembly and annual meeting (Abstracts)*.
780 https://inis.iaea.org/records/vdkrt-ern33.

781 Du Plessis, A., Le Roux, S. G., Guelpa, A. (2016). The CT Scanner Facility at Stellenbosch
782 University: An open access X-ray computed tomography laboratory. *Nuclear*
783 *Instruments and Methods in Physics Research Section B: Beam Interactions with*
784 *Materials and Atoms*, *384*, 42-49. https://doi.org/10.1016/j.nimb.2016.08.005.

785 Eckel, E.B. (1959) Geology and mineral resources of Paraguay - A reconnaissance. U.S. Geol.
786 Surv. Prof. Paper, 327:110p. https://doi.org/10.3133/pp327.

787 Ensikat, Hans., Malekhosseini, Mahdieh., Rust, Jes., Weigend, Maximilian. (2023).
788 Visualization of calcium oxalate crystal macropatterns in plant leaves using an
789 improved fast preparation method. Journal of microscopy. 290. 10.1111/jmi.13187.

790 Feng, D. (2022). *Visualizing inorganics in wood and wood composites using X-ray micro-*
791 *CT* (Doctoral dissertation, University of British Columbia). *Visualizing inorganics in*
792 *wood and wood composites using X-ray micro-CT* (Doctoral dissertation, University of
793 British Columbia). https://dx.doi.org/10.14288/1.0412782.

794 Frezzotti, M. L., Tecce, F., Casagli, A. (2012). Raman spectroscopy for fluid inclusion analysis.
795 *Journal of Geochemical Exploration*, *112*, 1-20.

796 Fúlfaro, V.F.; Saad, A.R.; Santos, M.V.; Vianna, R.B. (1982). Compartimentação e evolução
797 tectônica da Bacia do Paraná. Rev. Bras. Geoc., 12:590- 610.

798 Fúlfaro, V.J. (1996). Geología del Paraguay Oriental. Edusp/Fapesp, Sao Paulo, pp.17-29.
799 https://es.scribd.com/document/144463909/Geologia-del-Paraguay-Oriental.

800 García Gimenez,R.; Gil Sanchez, L.; Garcia Guinea, J. Y Leguey Jimenez, S. (1983).
801 Mineralogía de las maderas silicificadas de Palmaces de Jadraque (Guadalajara).
802 Boletín Sociedad Española de Mineralogía, pp. 115-122.
803 https://dialnet.unirioja.es/servlet/articulo?codigo=8796673.

804 Gavidia, G., Martín-Landrove, M., Cerrolaza, M. (2011). *Anatomía computacional: una*
805 *metodologia mejorada basada en imágenes médicas para la generación de modelos 3D*.
806 Barcelona. Center Internacional de Metodes Numerics en Eninyeria (CIMNE). ISBN
807 978-84-89925-48-9. http://hdl.handle.net/2117/99129.

808 Gee, C. (2013). *Applying MicroCT and 3D visualization to jurassic silicified conifer seed*
809 *cones: A virtual advantage over thin-section. Applic Plant Sciences 1 (11): 1300039*.
810 https://doi.org/10.3732/apps.1300039.

811 Géraud, Y., Surma, F., Mazerolle, F. (2003). Porosity and flow characterization of granites by
812 capillary wetting using X-ray computed tomography. In: Mees F., Swennen R. Geet
813 M.V., Jacobs P. (eds.) Aplications of x-ray computed tomography in geosciences.
814 London, Geological Society Special Publications, p.95-105.
815 https://doi.org/10.1144/GSL.SP.2003.215.01.09.

816 Gohrbandt, K.H.A. (1992). Paleozoic paleogeographic and depositional developments on the
817 central proto-Pacific margin of Gondwana: their importante to hydrocarbon
818 accumulation. J. South Amer. Herat Sci., 6:267-287. https://doi.org/10.1016/0895-
819 9811(92)90046-2.

820 Hales, F.W. (1980). An interpretation of the data from the airborne magnetic surveys in
821 northern areas of eastern Paraguay. Asunción, DRMMOPC/ LAC. 119p. (Relatorio
822 interno).

823 Harrington, H. J. (1950). Geología del Paraguay Oriental. Fac. Ci. Ex., Fis. Mat., Contr. Cient.,
824 Ser. E., Geología.
825 https://books.google.com.ar/books/about/Geología_del_Paraguay_Oriental.html?id=GZ
826 gkNAEACAAJ&redir_esc=y.

827 Herbst, R. (1972). Nota sobre la presencia de Lycopsidae arborescentes en el Pérmico (Serie
828 Independencia) del Paraguay. Ameghiniana, 9: 258-164.
829 https://ameghiniana.org.ar/index.php/ameghiniana/article/view/1389.

830 Herbst, R., (1981). Guairea Milleri novo gen. et sp. y Guaireacea, nueva Família de las
831 Osmundales (sensu lato) del Pérmico superior de Paraguay. Ameghiniana, 18 (1-2): 35-
832 50, Buenos Aires.
833 https://www.ameghiniana.org.ar/index.php/ameghiniana/article/view/1662.

834 Herbst, R. (1987). Studies on Psaroniaceae II. Tuvichapteris solmsi nov. gen et sp. from the
835 Permian of Paraguay and Uruguay. Actas del IV Congreso Latinoamericano de
836 Paleontología. Bolivia I: 267-287.

837 Herbst, R. & Leguizamon, R., (1984). La Formación Independencia (pérmico superior) del
838 paraguay: caracteres litológicos y paleontológioos. Facena (Corrientes, Argentina), 5:
839 71-87.

840 Ketcham, R. A., & Carlson, W. D. (2001). Acquisition, optimization and interpretation of X-ray
841 computed tomographic imagery: applications to the geosciences. *Computers &*
842 *Geosciences*, *27*(4), 381-400. https://doi.org/10.1016/S0098-3004(00)00116-3.

843 Kniss, J. M. (2002). *Interactive volume rendering techniques* (Doctoral dissertation, School of
844 Computing, University of Utah).
845 https://www.proquest.com/openview/c6ab7f2e4f50a326dd79b14a76bc8a56/1?cbl=1875
846 0&diss=y&pq-origsite=gscholar.

847 Leiva Verón. V, Crisafulli, A., Herbst, R., Filippi, V., Molina, S. (2012). Guavirá, una nueva
848 localidad con bosques fósiles de la Formación Tacuary del Pérmico Superior del
849 Paraguay. *Gaea: Revista de Geociencia*, *8* (2), 67.
850 http://dx.doi.org/10.4013/gaea.2012.82.04.

851 Li, Z., An, K., Yu, H., Luo, F., Pan, J., Wang, S., Zhang, J., Wu, W., Chang, D. (2024).
852 Spectrum learning for super-resolution tomographic reconstruction. *Physics in Medicine*
853 *& Biology*, *69*(8), 085018. https://doi.org/ 10.1088/1361-6560/ad2a94.

854 Litherland, M., Bloomfield, K. (1981) The Proterozoic history of Eastern Bolivia. Precambrian
855 Research, 15:157-179. https://doi.org/10.1016/0301-9268(81)90027-9.

856 Lozano Gutiérrez, R. E., Roque Romero, G. A., Ávila Rubio, C. D. (2018). MediPix3:
857 Evaluación de microtomografía de rayos X como método no destructivo para el estudio
858 de microanatomía comparada de maderas fósiles. http://hdl.handle.net/1992/39302.

859 Machado, A. S., Santos, R. S., Rodrigues, A. G., Borghi, L., de Oliveira, D. F., dos Anjos, M. J.,
860 Lopes, R. T. (2019). Characterization of carbonate rocks through X-ray
861 microfluorescence and X-ray computed microtomography. *X-Ray Spectrometry*, *48*(5),
862 543-552. https://doi.org/10.1002/xrs.3088.

863 Masschaele, B., Cnudde, V., Dierick, M., Jacobs, P., Van Hoorebeke, L., Vlassenbroeck, J.
864 (2007). UGCT: New X-ray radiography and X-ray tomography facility. Nuclear
865 Instruments and Methods in Physics Research, Section A: Accelerators, Spectrometers,
866 Detectors and Associated Equipment, 580 (1), 266-269.
867 https://doi.org/10.1016/j.nima.2007.05.099.

868 Matsunaga, K. K. S., Manchester, S. R., Srivastava, R., Kapgate, D. K., Smith, S. Y. (2019).
869 Fossil palm fruits from India indicate a Cretaceous origin of Arecaceae tribe Borasseae.
870 Botanical Jour nal of the Linnean Society, 190(3), 260–280.
871 https://doi.org/10.1093/BOTLINNEAN/BOZ019.

872 Muff, R., Gonzalez, M. E., Del Vergel, M. M., Herbst, R., Fasolo, Z. (1999). Palynological
873 investigations and biostratigraphic correlations of Permian sedimentary rocks from
874 eastern Paraguay. *Newsletters on stratigraphy*, *37*, 21-36.

875 Mustoe, GE (2017). Petrificación de la madera: una nueva visión de la permineralización y el
876 reemplazo. *Geosciences*, *7* (4), 119. https://doi.org/10.3390/geosciences7040119.

877 Mustoe, G. E. (2023). Silicification of wood: An overview. *Minerals*, *13*(2), 206.
878 https://doi.org/10.3390/min13020206.

879 Nowak, J., Florek, M., Kwiatek, W., Lekki, J., Chevallier, P., Zięba, E., Mestres, N.,
880 Dutkiewicz, EM., Kuczumow, A. (2005). Composite structure of wood cells in petrified
881 wood. *Materials Science and Engineering: C*, *25*(2), 119-130.
882 https://doi.org/10.1016/j.msec.2005.01.018.

883 Pakhnevich, A., Lychagina, T., Morris, S., Nikolayev, D. (2024). Local Crystallographic
884 Texture of Alpha Quartz in Silicified Wood (Late Triassic,
885 Madagascar). *Minerals*, *14*(11), 1128. https://doi.org/10.3390/min14111128.

Prasad, M., Lele, K. (1984). Triassic ginkgolean wood from the South Rewa Gondwana basin, India. Review of Palaeobotany and Palynology 40: 387- 397. https://doi.org/10.1016/0034-6667(84)90018-6.

Presser, J. L. B., Vladykin, N. V., Iwanuch, W. (2000). Lamproites of the Ybytyruzú Field, Guairá Department, Eastern Paraguay. In *Abstract of the 31st International Geological Congress. Rio de Janeiro: SBG* (pp. 1-1).

Rafferty, J. P. (Ed.). (2011). Britannica Educational Publishing. series=Geology: Landforms, Minerals, and Rocks. ISBN=9781615305827. https://books.google.com.ar/books?id=MB9XNiP4sagC.

Raman, C.V. (1928). A new radiation. Indian Journal of Physics. Vol.2, p. 387. https://www.jstor.org/stable/24101519.

Rapalini, A.E.; S. Fazzito., D. Orue. (2006). A new Late Permian paleomagnetic pole for stable South America: The Independencia Group, Eastern Paraguay. Earth, Planets and Space, 58, 1247-1253. https://doi.org/10.1186/BF03352620.

Runnegar, B., Newell, N. (1971). Caspian-like relict molluscan faunain the South American Permian. Bull. Amer. Mus. Nat. Hist., 146: 66p.

Sabella, P. (1988). A rendering algorithm for visualizing 3D scalar fields. In *Proceedings of the 15th annual conference on Computer graphics and interactive techniques* (pp. 51-58). https://doi.org/10.1145/54852.378476.

Schneiders, R. (1996). A grid-based algorithm for the generation of hexahedral element meshes. *Engineering with computers*, *12*, 168-177. https://doi.org/10.1007/BF01198732.

Salehjahromi, M., Zhang, Y., Yu, H. (2017). Un algoritmo de eliminación de ruido de TC espectral basado en el filtrado 3D de coincidencia de bloques ponderados. En *Developments in X-Ray Tomography XI* (Vol. 10391, págs. 65-76). SPIE. doi:10.1002/mp.13762.

Salehjahromi, M., Zhang, Y., Yu, H. (2018). Comparison study of regularizations in spectral computed tomography reconstruction. *Sensing and imaging*, *19*, 1-23. https://doi.org/10.1007/s11220-018-0200-4.

Saminpanya, S., Ratanasthien, B., Jatusan, W., Limthong, R., Amsamarng, T. (2024). Mineralogy, geochemistry, and petrogenesis of the world's longest petrified wood. *International Journal of Geoheritage and Parks*, *12*(1), 37-62.

Staedler, Y. M., Masson, D., Schönenberger, J. (2013). Plant tissues in 3D via X-ray tomography: simple contrasting methods allow high resolution imaging. *PloS one*, *8*(9), e75295. https://doi.org/10.1371/journal.pone.0075295.

Sutton, M. D. (2008). Tomographic techniques for the study of exceptionally preserved fossils. *Proceedings of the Royal Society B: Biological Sciences*, *275* (1643), 1587-1593. https://doi.org/10.1098/rspb.2008.0263.

924 Vallejos Leiz, L., Crisafulli, A., Herbst, R. (2018). Siraty, una nueva localidad fosilífera con
925 maderas y estípites de la Formación Tacuary (Pérmico superior), Paraguay. *Revista del*
926 *Museo Argentino de Ciencias Naturales*, *20*(2), 283-296. Recuperado en 26 de febrero
927 de 2025, de https://www.scielo.org.ar/scielo.php?script=sci_arttext&pid=S1853-
928 04002018000200008&lng=es&tlng=es.

929 Vega, Sandra., Carrasco-Núñez, Gerardo & Arteaga, Dante., Cid, Hector E., Manea, vlad
930 constantin. (2018). Microtomografía de rayos X: preparación de muestras de rocas para
931 una mejor visualización y caracterización del espacio poroso. Revista NTHE. Vol. 20.
932 Pp. 25-32.
933 https://www.researchgate.net/publication/327273622_Microtomografia_de_rayos_X_pr
934 eparacion_de_muestras_de_rocas_para_una_mejor_visualizacion_y_caracterizacion_de
935 l_espacio_poroso.

936 Velázquez, V., Gomes, C., Orué, D., CominChiaramonti, P. (1996). Magmatismo alcalino do
937 Paraguai: uma revisão e atualização das Províncias. Boletim do Instituto de Geociências
938 – USP (Série Científica), 26: 61–79. https://doi.org/10.11606/issn.2316-8986.v27i0p61-
939 79.

940 Viney, M., Dietrich, D., Mustoe, G., Link, P., Lampke, T., Götze, J., Rößler, R. (2016). Multi-
941 stage silicification of Pliocene wood: Re-examination of an 1895 discovery from Idaho,
942 USA. *Geosciences*, *6*(2), 21. https://doi.org/10.3390/geosciences6020021.

943 Vinegar, H. J. (1986). X-ray CT and NMR imaging of rocks. *Journal of petroleum*
944 *technology*, *38*(03), 257-259. https://doi.org/10.2118/15277-PA.

945 Wang, Y., Wang, G., Mao, S., Cong, W., Ji, Z., Cai, J. F., Ye, Y. (2016). A framelet-based
946 iterative maximum-likelihood reconstruction algorithm for spectral CT. *Inverse*
947 *problems*, *32*(11), 115021. https://doi.org/10.1088/0266-5611/32/11/115021.

948 Wellington, S. L., Vinegar, H. J. (1987). X-ray computerized tomography. *Journal of petroleum*
949 *technology*, *39*(08), 885-898. https://doi.org/10.2118/16983-PA.

950 Wiens, F. (1982). Mapa geológico de la región oriental. República del Paraguay, escala 1:
951 500,000. Sim. Rec. Nat. Paraguay. Asunción, 9p.

952 Wiens, F. (2018). Potencial de Hidrocarburos del Paraguay. Tomo I.
953 https://www.researchgate.net/publication/326211410_Potencial_de_Hidrocarburos_del_
954 Paraguay_TOMO_I.

955 Witke, K., Götze, J., Rößler, R., Dietrich, D., Marx, G. (2004). Raman and
956 cathodoluminescence spectroscopic investigations on Permian fossil wood from
957 Chemnitz a contribution to the study of the permineralisation process. *Spectrochimica*
958 *Acta Part A: Molecular and Biomolecular Spectroscopy*, *60*(12), 2903-2912.
959 https://doi.org/10.1016/j.saa.2003.12.045.

960 Yu, Kuanhong; Du, Shuo; Cao, Yingchang; Zhang, Tao. (2024). Opaline silica precipitations in
961 the Permian Fengcheng Formation indicate hot spring environments in north Mahu Sag,
962 NW China. Marine and Petroleum Geology. Volume 166. 106924.
963 https://doi.org/10.1016/j.marpetgeo.2024.106924.

Supplementary Files

This is a list of supplementary files associated with this preprint. Click to download.

- SupplementaryInformationBaezetal.docx